Angle-resolved transmission spectroscopy of opal films

M. Muldarisnur,[1] I. Popa,[1] and F. Marlow[1,2,*]

[1]*Max-Planck-Institut für Kohlenforschung, Kaiser-Wilhelm-Platz 1, 45470 Mülheim an der Ruhr, Germany*

[2]*Center for Nanointegration Duisburg-Essen (CeNIDE), University of Duisburg-Essen, Germany*

(Received 14 December 2011; revised manuscript received 2 March 2012; published 16 July 2012)

The angular behavior of light transmission through opal films over a broad range of wavelengths and angles was investigated. The opal films were prepared using the capillary deposition method (CDM). Many well-defined diffraction peaks were detected and indicate that the CDM results in opal films with high quality. Peaks coinciding at normal incidence split when samples are rotated. The angular shift of these peaks was found to satisfy the kinematical diffraction theory very well. Furthermore, the variation of intensity with incident angle can be interpreted in terms of a simplified dynamical diffraction theory. Moreover, the presence of two differently oriented domains in CDM-made opal films is essential in discussing the measured spectra.

DOI: 10.1103/PhysRevB.86.024105 PACS number(s): 42.70.Qs, 78.67.Pt, 07.60.Rd, 81.16.Dn

I. INTRODUCTION

The optical response of photonic crystals at frequencies above the well-known stop band is of a special interest due to rich optical phenomena and their related applications. Slow-light-enhanced light-matter interactions at flat bands in this region can, for example, improve the performance of all applications where optical gain, absorption, and nonlinear effects are necessary.[1] Furthermore, the engineering of refraction phenomena, e.g., self-collimation,[2] superprism effects,[3,4] and negative refraction,[5] are steps towards all-optical integrated circuits.

Due to the statistical nature of self-assembly processes, the resulting artificial opals contain many defects (point defects, dislocations, twin boundaries, and domains) that are not well understood. Scattering by defects is believed to be one reason for peak broadening and background in the measured spectra.[6–8] These effects decrease the resolution and signal-to-noise ratio of high-order peaks severely at short wavelength. As a consequence, high-quality opals are necessary to study optical properties in this wavelength range.

Surprisingly, there is only a limited number of works on the interpretation of transmission (or reflection) spectra at frequencies above the stop band.[9–17] Published works[12–18] mainly attempted to explain special features like the observed double peak of the stop band at the edge of the Brillouin zone. The observed peaks have been interpreted using different concepts: overlap of Bragg diffractions,[12–14] band branching,[15] twinning,[16,17] and surface diffraction.[18] Many of them point out the "mixing" of the different diffraction planes. In the twin-based interpretation,[16,17] two possible beam paths are discussed. The first one is the normal Bragg reflection, but the second one comes from the reflection of refracted light in the opal by two fcc twins. The two beams have a similar direction and are detected simultaneously.

Frequently, transmission (or reflection) spectra have been compared with band structure calculations.[12,19,20] This approach perfectly describes the angular behavior of the stop band. At higher frequencies, however, the observed peaks are more difficult to interpret; in this region, many bands exist[21] and intermix.[22] The correspondence between band structure and transmittance (or reflectance) spectra is still a matter of debates.

It seems that Lopez *et al.*[22] were the first to use the concept that dips in transmission spectra originate from diffracted beams that are not collected by the detector. The interpretation based on diffraction was refined by Andreani *et al.*[10,23] and Nair *et al.*[24] by calculating the density of states along a certain propagation direction called directional DOS. They found out that the stop band and the second-order peak, respectively, correspond to a dip and a sharp peak in the directional DOS. Míguez *et al.*[11] suggested that the low group velocity of flat bands can be the origin of high reflectivity at high frequencies. Unfortunately, there was no further discussion why peaks were observed only at certain frequencies. Peak assignment based on Bragg diffraction for liquid-infiltrated opals was reported by Rybin *et al.*[25] and Asher *et al.*[26]

In this paper, we describe the rich features in angle-resolved transmission spectra showing various angular dependences. The measured spectra are interpreted based on a nonstandard combination of kinematical and dynamical diffraction theories. The presence of oriented domains of different fcc lattices was found to be reflected in the measured spectra.

II. EXPERIMENTAL PART AND NUMERICAL DETAILS

A. Sample preparation

Thin opal films were prepared by using the capillary deposition method (CDM). Details of this method have been described before.[27,28] A 0.5 wt% suspension was obtained by diluting a 10 wt% suspension (Microparticles GmbH) of polystyrene spheres (diameters: 920 ± 23 nm and 266 ± 7 nm) with Milli-Q water. The dilution process was carried out with the assistance of an ultrasonic bath to ensure the suspension homogeneity. The thicknesses of polymer spacers (Pütz GmbH + Co. Folien KG) determining thickness of resulting opal films were 15, 25, and 50 μm. Opal deposition was carried out at 23 °C and 35% RH in a room with well-regulated temperature and humidity. Deviations in temperature and relative humidity were in the range of ± 1 °C and $\pm 1.5\%$, respectively. Depending on thickness, it took 2–5 days for opal deposition to be complete.

Colloidal particles with a big diameter were chosen in order to obtain higher-order diffraction within a range of wavelength where the spectrometer works well. For wavelengths lower

than 400 nm, material absorption reduces the resolution of the measured spectra. The opal film with a particle diameter of 266 nm was prepared for optical microscopy imaging.

B. Characterization

The transmission measurements of the opal films were carried out using a Cary 5G UV/vis-NIR spectrometer (Varian). A variation of the incident angle of incoming beam was achieved by employing a rotating stage (C-862 Mercury, Physik Instrumente GmbH) for rotating the opal samples. The stage was placed in the middle of the sample container of the spectrometer. Opal films were positioned on top of the rotating stage at a distance of about 8 cm from the incoming light entrance. The spot size was approximately 15×3 mm^2. The measurements were accomplished by synchronizing the transmission measurement and the stage rotation in a cyclic mode. The measurement time of each cycle was divided into scanning and idle times. After scanning at a certain incident angle, the opal sample was rotated to the next intended angle within the idle time. In all measurements, the times to rotate the stage were much shorter than the idle times ($t_{\text{rotate}}/t_{\text{idle}} < 1/50$). An angular resolution better than 1 millidegree was achieved using this rotating stage.

Angle-resolved transmission spectra were measured for two scanning directions with respect to the opal growth direction, **g** (see Fig. 1). The two cases differ in respect to the orientation of rotation vector ($\boldsymbol{\omega}$) and growth direction. In the setup labeled V, $\boldsymbol{\omega}$ is perpendicular to **g**, whereas for the setup H they are parallel to each other. The spectra were taken at a wavelength range between 400–2500 nm (step 1 nm) with an angular variation from -70° to 70° (step 1°). The detector of the spectrometer changed at 800 nm from PbS photocell for NIR to photomultiplier for UV-Vis. This change caused a small step ("kink") of the extinction especially for scattering samples. The baseline correction measurements were performed without any sample.

A stereomicroscope (Nikon SMZ-1B, objective 3.6×2x, working distance 4 cm) was used for the observation of domains in the opal films. Dark-field imaging of opal samples was performed with illumination from Halogen light source (Schott KL1500 LCD). Light guiding with two flexible fiber-optics allowed easy manipulation of incoming light inclination. The guides were fixed to shine the samples symmetrically from left and right at an angle of about 45° with respect to the surface of opal films and at an angle of about 100° to the growth direction. Images were taken at a low objective magnification (1.0×2x) by mounting a microscope digital camera MA88 (C & A Scientific Co., Inc.). At image acquisition, the position of the camera was chosen to be on the opposite side of incoming light. Changing the camera position caused a slight shift of the probed area. The initially imaged area was restored by moving the sample carefully.

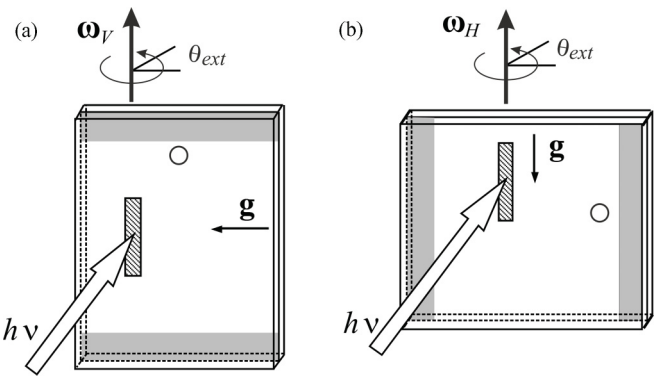

FIG. 1. Opal orientation for angle-resolved spectroscopy (ARS) measurement (a) case V, (b) case H. The shaded regions show parts of the samples where measurements were preformed. The angle $\theta_{\text{ext}} = 0$ is normal incidence.

C. Simulations

The band structure calculations of opals were carried out by using the MPB program (MIT photonic bands)[29] which is freely available online. All calculations for different packing conditions (i.e., sintered, close-packed, and expanded opals) were done for polystyrene opals with a refractive index of 1.59. The grid size and resolution were 7 and 32, respectively. The resolution defined the number of plane waves used for calculation. The sintered opal was approximated by overlapping spheres.

III. RESULTS

A. ARS maps

Angle-resolved spectroscopy (ARS) allows the tracking of spectral features of opal films upon changing the incident angle. The observed peaks can be more confidently assigned to systematic variations from ARS than just based on spectra at the single angle $\theta_{\text{ext}} = 0$. Figure 2(a) shows the shift of the first-order peak corresponding to the stop band. Initially, the peak occurs at 2 μm and then it shifts to a shorter wavelength

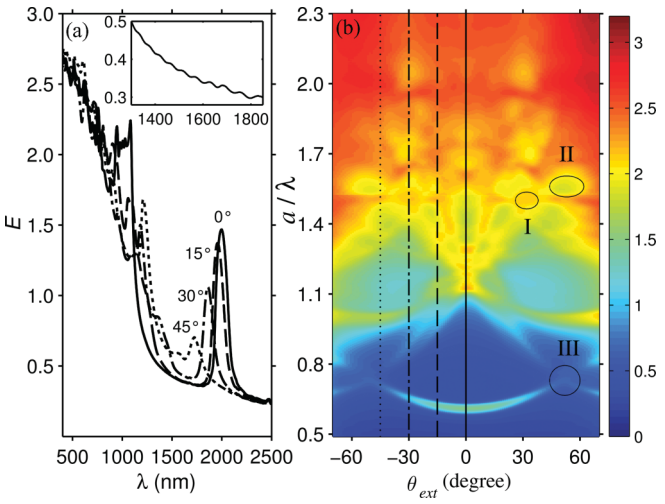

FIG. 2. (Color) (a) Extinction spectra for selected incident angles and (b) ARS map for the case H (sample: MDN-MA-102-02). The spectra in (a) are the cuts of the ARS map along the indicated lines. The inset is the zoom of the transmittance spectrum at normal incidence showing Fabry-Perot oscillations. Descriptions of the features I, II, and III are given in the text. The scale of color bar will be used in all following ARS maps.

as the incident angle increases. Also Fabry-Perot oscillations are noticeable (inset).

Shifts and the intensity variations have also been reported in many other works (see, e.g., Refs. 12, 15, 16, 20, and 21). However, the features at short wavelengths cannot be identified easily. They may come from diffraction by the lattice planes or simply from noise. When presented in an ARS map as in Fig. 2(b), however, these complicated features become a remarkably pronounced pattern.

An ARS map is a surface plot of the extinction ($E = -\log_{10} T$) versus frequency and the external incident angle. Due to the elongated shapes of extinction peaks in this presentation, we will call them "ridges" and the region in-between "pans," respectively. The normalized frequency is used in the ARS maps because the Maxwell equations become scale-invariant using this frequency, $\tilde{\omega} = \omega a/2\pi c = a/\lambda$. Here, it is expressed by the wavelength in vacuum λ and the fcc lattice constant a. The second basic parameter in the ARS map is the external angle θ_{ext} of the incident light with respect to the normal of the surface of the opal film.

Several ridges at $\tilde{\omega} = 1, \ldots, 1.3$ that overlap at normal incidence clearly split in the ARS map due to the different angular dependence of these peaks. The crossing of the two lowest-order ridges at an angle of about 55° (at $\tilde{\omega}$ of about 0.7) becomes also easily visible.

Even above $\tilde{\omega} = 2$, a number of well-resolved ridges becomes visible in the ARS maps (see Fig. 3). A single ridge describes an extinction peak shifting with a special angular dependence. Every ridge occurs in both cases (V and H), but with different slope and position, as it will become clear later.

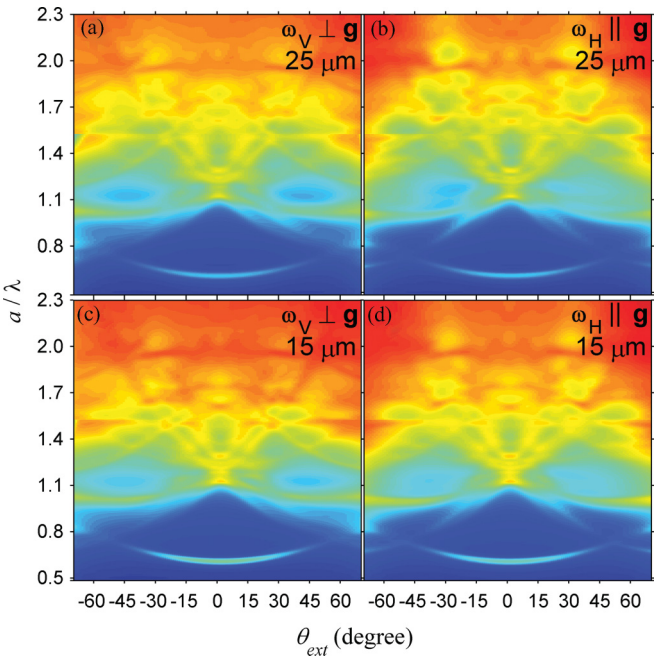

FIG. 3. (Color) (a) and (b) ARS maps of sample MDN-MA-098-02 with 25 μm thickness for case V and H as indicated. (c) and (d) ARS maps of sample MDN-MA-102-02 (different position as in Fig. 2) with 15 μm thickness for case V and H. All ARS maps use the same scale of color bar as in Fig. 2. Although the H and the V map are qualitatively very similar, there are reproducible shifts in the band crossings and transmission eye positions.

To our knowledge, no previous work has reported such a high resolution of extinction peaks for frequencies $\tilde{\omega} > 1.2$, likely due to the quality of the samples used.

B. Special features

In the high-frequency region, the ARS maps show complicated patterns due to crossing of ridges (Fig. 2, feature I). The most notable crossings are at $\tilde{\omega} = 1.5$ and 1.7 with corresponding θ_{ext} of about ±25° and ±15° for case V. For case H, the crossings appear at slightly larger angles, at about ±30° and ±20°. At these crossings, simultaneous diffraction occurs at different lattice planes (called "multiple" diffraction by Vos *et al.*[13,14]). This could be of interest for beam splitting or mixing processes. Furthermore, quite narrow regions of reduced extinction are visible which might be called transmission eyes (feature II). Those could be used for efficient propagation through the photonic crystal and for excitation of electronic or other nonphotonic states.

The lowest-frequency crossing of two peaks (feature III) is worth to be discussed more in detail (see Sec. IV). The experimental findings show that the crossing angle is smaller in case H than in case V and that the crossing point is more pronounced in case H.

The height of the ridges in the ARS maps shows also a pronounced variation. The stop band (at $\tilde{\omega} = 0.603$ for normal incidence) can be described by a monotonous decrease whereas the ridge at $\tilde{\omega}$ about 0.9–1.1 has an initial decrease followed by an increase with the increasing incident angle. The intensities of many other ridges at frequencies above 1.1 are less changing upon change of incident angle. These nearly flat ridges are, for example, visible at frequencies of about 1.5 and 1.9.

Additionally, we mention the following: (i) The kink at $\tilde{\omega} = 1.52$ (equivalent to $\lambda = 800$ nm) is a result of changing the detector. The kink is more pronounced at incident angles above 40 degrees. (ii) The ARS maps for opals with thicknesses of 15 μm and 25 μm show no significant differences. Also an opal with a thickness of 50 μm has a very similar pattern, but the strong background reduces the contrast between ridges and pans for $\tilde{\omega} > 1.2$. (iii) Less-resolved ridges can be noticed for case H at frequencies above 1.7 and angles larger than 40 degrees. They probably occur due to the inclusion of the middle region that contains a high concentration of defects (see, e.g., the title picture of Ref. 30).

C. Lateral structure

Besides the spectral and angular behavior, the lateral homogeneity is an interesting question. Since it is convenient to do these investigations in the visible range, we used smaller spheres for that. When viewing in reflection with the naked eye, an opal sample (diameter 266 nm) shows metallic-red appearance at normal incidence. It looks greenish and bluish at oblique viewing angles. The opalescence is homogeneous over the whole sample area.

A microscope observation, however, surprisingly reveals the existence of regular stripes showing different brightness. The stripes cover most of the sample area. The stripes look either bright greenish or dark with slightly red colors

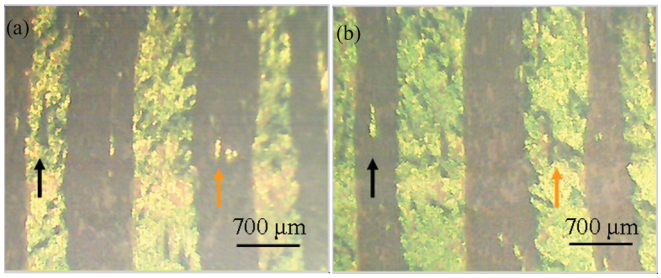

FIG. 4. (Color) Dark-field images of an opal sample viewed under a stereomicroscope (objective 1.0 × 2x, working distance 4 cm) with illumination at ∼45° from left (a) and right (b). The arrows with the same color indicate the same features.

depending on the incoming beam direction. Dark-field images of a representative area are shown in Fig. 4. The left image was taken with illumination from the left. When the beam came from the right, the initially bright area turned dark and vice versa as is shown in Fig. 4(b). Some smaller regions appearing dark in the bright stripes were also nicely inverted between left and right images.

The width of one stripe varies from sample to sample, it even varies within one sample. In general, its value is between 400 and 1500 μm. The average stripe width is around 700 μm, which is much bigger than the crack distance (50–100 μm) typical for CDM- and VD-made samples.[27,28]

IV. DISCUSSION

A. Scanning planes

The knowledge of lattice orientation[28] of CDM-made opal films in respect to the growth direction allows the determination of the scanning planes in the **k** space. Since the growth direction $\mathbf{g} = [1\bar{1}0]$, the rotation vectors shown in Fig. 1 are $\boldsymbol{\omega}_V = \mathbf{n} \times \mathbf{g} = [11\bar{2}]$ and $\boldsymbol{\omega}_H = \mathbf{g} = [1\bar{1}0]$. The opal film surface is oriented perpendicularly to $\mathbf{n} = [111]$ in the conventional choice of the coordinate system. The scanning planes (see Fig. 5) are perpendicular to the rotation vectors. These planes are probed by the beam in an angle-resolved experiment.

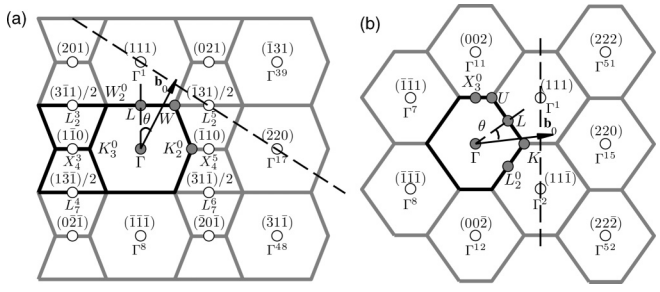

FIG. 5. Scanning planes for (a) case V and (b) case H. The order of the superscript of the different Gamma points was chosen with increasing distance to Γ and due to an appropriate *hkl* ordering. The dashed lines are special scanning lines for (022)-type ridges that will be discussed in Secs. IV C and IV D.

Figure 5 displays the reciprocal lattice including the higher BZs. To show the relation between the lattice points outside and inside the first BZ, they are labeled in the following manner: $X_m^n = X_m^0 + \Gamma^n$ and $L_m^n = L_m^0 + \Gamma^n$ with the subscript m for the different X or L points inside one BZ and the superscript n for the different BZs. For the points of the irreducible BZ we use $\Gamma = \Gamma^0$, $L = L_1^0$, $X = X_1^0$, etc., as usual. According to this drawing, the variation of the external angle for case V corresponds to the scanning along the $K_3^0 W_2^0 L W_1^0 K_2^0$ path regarding the edge of the lowest BZ. For case H, it corresponds to scanning along $X_3^0 U L K L_2^0$. For ideal polystyrene opal, W and $K(U)$ points correspond to the external incident angles 64° and 56°, respectively.

B. Kinematical interpretation of the ARS maps

A direct comparison of the ARS map with the band structure shows a matching only for the ridge corresponding to the lowest stop band.[31] A fair agreement can be obtained for the ridge at $\tilde{\omega} \sim 0.9$–1.1 in case H by introducing slight corrections (i.e. sphere deformation) into the calculated model. Above this frequency, no coincidence has been found between band structures and spectra. Therefore we propose to use a kinematical picture first, in order to assign the peaks (ridges) in the complicated patterns of the ARS maps. In the kinematical picture as used in crystallography,[32] the extinction peaks originate from diffraction at lattice planes. This picture is rough for photonic crystals, but it might be helpful to clarify the origin of the extinction maxima.

The wavelength corresponding to diffraction by the (*hkl*) plane can be calculated by using the Bragg law:

$$\lambda_{hkl} = 2 n_{\text{eff}} d_{hkl} \cos\theta_{hkl}, \tag{1}$$

where $n_{\text{eff}}, d_{hkl}, \theta_{hkl}$ are the effective refractive index, the interplanar distance, and the angle between (*hkl*) and the beam, respectively. The effective index of the opal can be approximated by the volume-averaged refractive index of constituent materials, $n_{\text{eff}} = n_{\text{sph}}\phi_v + (1 - \phi_v) n_m$, with the refractive index of the particles (n_{sph}), the refractive index of the medium (n_m), and the particle filling fraction ($\phi_v = V_{\text{sph}}/V$). The interplanar distance is $d_{hkl} = D\sqrt{2}(h^2 + k^2 + l^2)^{-1/2}$, with the diameter of colloidal particles D. In this work, the effective refractive index and the lattice constant were simultaneously determined by fitting of the angular λ_{111} behavior.

To calculate θ_{hkl} from the external observation angle θ_{ext}, we determine the beam direction vector $\mathbf{b}_0$ first. The refraction at the surface of the opal is taken into account using Snell's law to calculate the internal angle:

$$\theta_{\text{int}} = \sin^{-1}(\sin\theta_{\text{ext}}/n_{\text{eff}}). \tag{2}$$

Then, the beam direction vector is

$$\mathbf{b}_0 = \mathbf{n} + \tan(\theta_{\text{int}}) \cdot (\mathbf{n} \times \boldsymbol{\omega}^{\#}), \tag{3}$$

where $\boldsymbol{\omega}^{\#} = \boldsymbol{\omega}_{V/H}/|\boldsymbol{\omega}_{V/H}|$ is the normalized rotation vector either for case V or for case H. This vector can finally be used for calculating θ_{hkl}:

$$\theta_{hkl} = \cos^{-1}\left[\frac{(\mathbf{b}_0 \cdot \mathbf{G}_{hkl})}{|\mathbf{b}_0|\,|\mathbf{G}_{hkl}|}\right]. \tag{4}$$

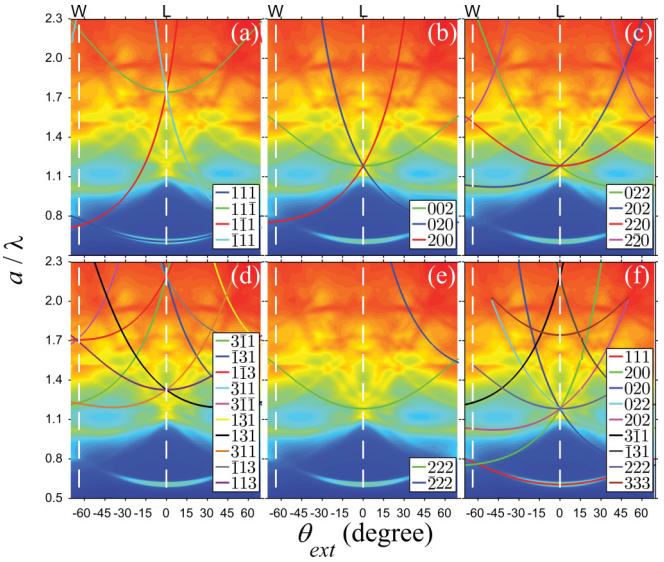

FIG. 6. (Color) ARS map with calculated lines for different families of diffraction planes for case V: (a) {111}, (b) {002}, (c) {022}, (d) {311}, (e) {222}, and (f) selected lines for all families including {333}.

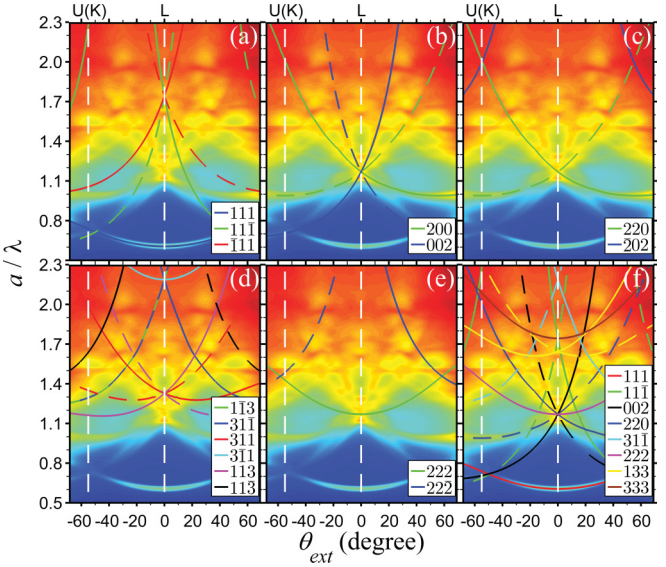

FIG. 7. (Color) ARS map with calculated peaks for different families of diffraction planes for case H. (a) {111}, (b) {002}, (c) {022}, (d) {311}, (e) {222}, and (f) selected peaks for all families including {331} and {333}. The dashed lines are mirror images of solid lines with respect to the $\theta_{\text{ext}} = 0$ line.

The calculation of θ_{hkl} with Eqs. (2)–(4) is more general than similar approaches reported before by other authors.[15,33] It is valid for all diffraction vectors, not only for those on the scanning planes.

Due to the fact that the refractive index of PS varies with the wavelength, the solution of Eq. (1) cannot be obtained in a straightforward manner. For a given θ_{ext}, the values of θ_{hkl}, $\mathbf{b}_0$, and θ_{int} in Eqs. (1)–(4) slightly depend on the Bragg wavelength, which we want to calculate. However, since this dependence is weak, Eqs. (1)–(4) can be solved iteratively.[31]

In Figs. 6 and 7, the calculated angular variation of the Bragg wavelength of different *hkl* planes is overlapped with the measured spectra. We note that many lines from different planes in one family are identical and, thus, only one of them is shown. Some lines lie above the regarded frequency range; therefore, they are not visible.

Figure 6(a) shows a perfect agreement of the (111) diffraction line with the measured ridge over the whole angular range. The other lines have no coincidence with experimental features. All diffraction lines from {002} planes are in perfect agreement with the ridges in the ARS map as shown in Fig. 6(b). Very good agreement is visible for {022} planes except for the $(2\bar{2}0)$ plane, which is difficult to judge because it is located in the region of high background. For the {113} planes [see Fig. 6(d)], good agreements are evident only for $(3\bar{1}1)$ and $(\bar{1}31)$ planes. Perfect agreement was found only for the (222) plane in Fig. 6(e). All nonidentical diffraction lines that are in good agreement with measured ridges are compiled in Fig. 6(f).

It is noticeable that several calculated diffraction lines [e.g., $(\bar{1}11)$,(113), and $(22\bar{2})$] are not observed in the ARS map. Some of these disappearances can be explained with small form factors [e.g., for the (002)- and (222)-type reflections], others cannot. Their disappearance is beyond the kinematical picture. In addition, one observes pronounced intensity variations along all diffraction ridges, which have also no explanation in this picture. These phenomena will be considered in the next section.

Apart from the appearance or disappearance of reflections in ARS maps, there are slight discrepancies in the position of some reflections. We ascribe them to the applied effective refractive index, which must be considered as a rough approximation for the behavior of waves in the opal. To improve fitting, we slightly generalize the effective refractive index approximation that was used up to now. The effective medium theory that was essentially developed for small scatterers (or long wavelength) approaches its validity limit in opal systems. The ratio of the scatterer size to the wavelength of light is about one or even larger. We propose to correct this by introducing a wavelength-dependent correction through a field occupation factor $\phi_f = e_{\text{sph}}/\bar{e}$, relating the energy densities in the spheres with the average energy density. Then, the volume filling fraction ϕ_v should be replaced by $\phi = \phi_v\phi_f$ that represents the degree of field energy concentration in the dielectric (spheres). Above 1 μm, the ϕ_f was found to be equal to one (no correction). It increases by about 10% at shorter wavelengths. That means that at high frequencies the average field of the propagating waves is slightly stronger inside the dielectric compared to the air regions. This correction is already included in Figs. 6 and 7.

The dashed lines in Fig. 7 were added as mirror images of the corresponding lines with the same color. This addition was made due to the fact that our CDM-made opals contain two different mirror-symmetric domains that were simultaneously probed by the incoming beam. Subdomain spectroscopy[19,34] might be of interest to see differences in their optical properties. However, it should be noted that most of these mirror images overlap with other lines in the family.

Theoretically, the variation of the incident angle to positive or negative values is asymmetric in case H. The scan includes, e.g., states at the L_2^0 point for positive angles and states at X_3^0

for negative angles. They correspond to the $(11\bar{1})$ and the (002) reflection, respectively, in the kinematical picture. The states as well as the reflections are clearly different and therefore a difference in the spectra can be expected. Because of that, the observed symmetry of the ARS map in the case H can be assigned as an effect of the simultaneous probing of the two different fcc domains.

In Fig. 7(a), a perfect matching is visible for the (111) and the $(11\bar{1})$ planes. The other reflections of this family are not observed experimentally. For {002} planes, perfect agreement was found for the (002) and the (200) planes. In Fig. 7(c), the (220) fits nicely with the corresponding ridge. In Fig. 7(d), good agreements were found only for the $(1\bar{1}3)$ and the $(31\bar{1})$ planes, which are mirror images of each other. Perfect agreement was found also for the (222) peak as shown in Fig. 7(e). All nonidentical peaks that are in agreement with the measured ridges are compiled [see Fig. 7(f)].

C. Kinematical interpretation and band structures

In the last section, the Bragg law was used to calculate the $\tilde{\omega}(\theta_{\text{ext}})$ positions of diffracted beams. However, this calculation delivers neither the width of the diffraction peaks nor the dependence of their intensity on the incident angle. However, both are apparent in ARS maps. This information is beyond the kinematical picture but it can partially be extracted from the band structure.[35] Normally, this information is obtained by considering the partial band gaps and the coupling efficiencies of the different modes with free waves. However, a simplified interpretation based on the band structure can already deliver the main features.

What exactly is the correspondence between the kinematical picture and the band structures? In the kinematical picture, the reduced extinction is caused by scattering, which occurs when the k vector is on a Bragg plane defined by $\mathbf{k} \cdot \mathbf{G} = |\mathbf{G}|^2/2$.[36] The frequency of the scattered light is then given by the light cone formula $\omega = |\mathbf{k}|c/n_{\text{eff}}$. Compared to that, the band structures describe the allowed propagation states. In band gaps no propagation is possible; therefore the band edges are connected with the edges of the extinction peaks. Band edges can preferentially be found at symmetry planes in inverse space. If the symmetry plane is identical to a Bragg plane, both ways of interpretation correspond to each other.

Practically, this correspondence is easy for the (111) ridge. The Bragg plane is the edge of the lowest BZ, therefore the band structure at the plane containing *LUKW* corresponds to this reflection. For the (022) ridge, however, the Bragg plane contains $\Gamma^1\Gamma^2$ [see Fig. 5(b)], so it is not an edge of a BZ anymore. The band structure has to be calculated along this line and the relevant bands are those surrounding the light cone.

D. Extinction intensities

We describe the measured extinction peaks in terms of the frequency-integrated transmission drop intensity [$I_{\text{TD}} = \int d\tilde{\boldsymbol{\omega}}(\boldsymbol{T}_{\text{BG}} - \boldsymbol{T})$], the simplest information not exploiting a special shape of the peak (see Fig. 9). The background in the measured spectra ($E_{\text{BG}} = -\log_{10} T_{\text{BG}}$) has to be determined and separated prior to integration. The increase of background with angle was approximated by $E_{\text{BG}} = E_0/\cos\theta_{\text{int}}$. Since the transmission drop inside the band gap is nearly constant, the I_{TD} is approximately proportional to the width of the gaps. This enables comparison with the band structure.

We focus on the discussion of three ridges [(111), (022), and (220)] showing a strong angular variation in their height. The theoretical width of the (111) ridge can be obtained directly from the known band structure along the edge of the lowest BZ. However, this is not the case for the (022)-type ridges as discussed in Sec. IV C. The Bragg planes lie outside of the lowest BZ. For calculation, we first determine the scan lines (crossing of scan plane and Bragg plane) and the corresponding external angles. Figure 5(b) shows that this line is $\Gamma^1\Gamma^2$ in case H. By knowing that the internal angle $\angle(\Gamma^1\Gamma X_3^2)$ is equal to $\angle(L\Gamma K)$, the external angles can be calculated from the k points of the MPB output (see Sec. II C). From Fig. 8(b), one can see that the gap between the 6th and the 8th bands corresponds to this ridge. The 7th band is either equal to the 6th or the 8th bands. For the case V, the scanning line is not so easy to see because the (022) point lies outside of the scanning plane shown in Fig. 5(a). However, closer geometrical considerations show that the scanning line contains Γ^1 and Γ^{17} [drawn in Fig. 5(a)]. Therefore, the band structure was calculated there as visible in Fig. 8(a). A magnified view of this figure shows that the light cone lies between the 8th and the 9th bands.

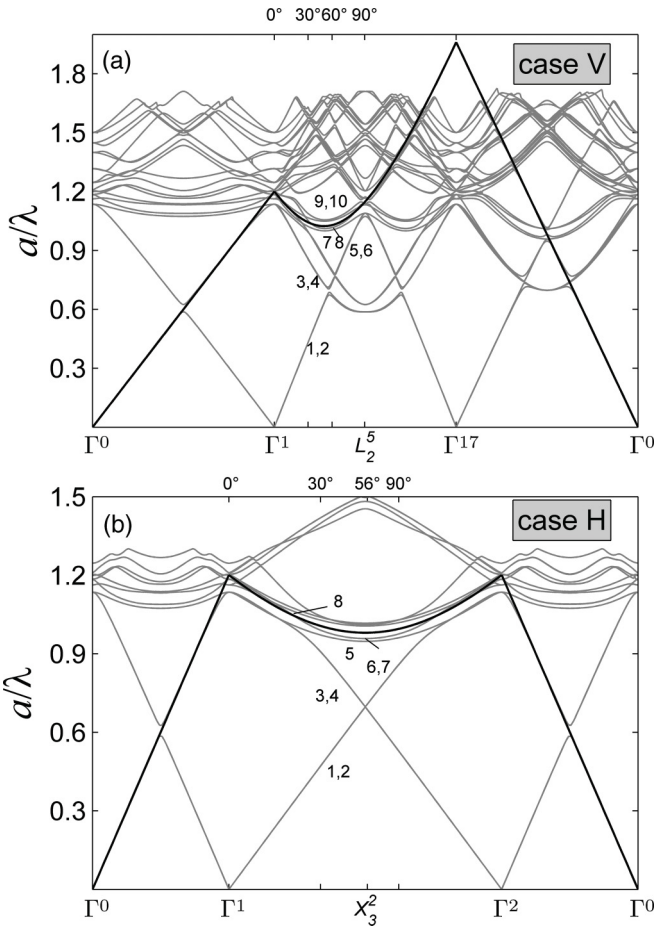

FIG. 8. Band structure at the scanning lines (a) $\Gamma^1\Gamma^{17}$ and (b) $\Gamma^1\Gamma^2$. The black lines are the corresponding light cones. Some selected external angles are given on the top of the plots.

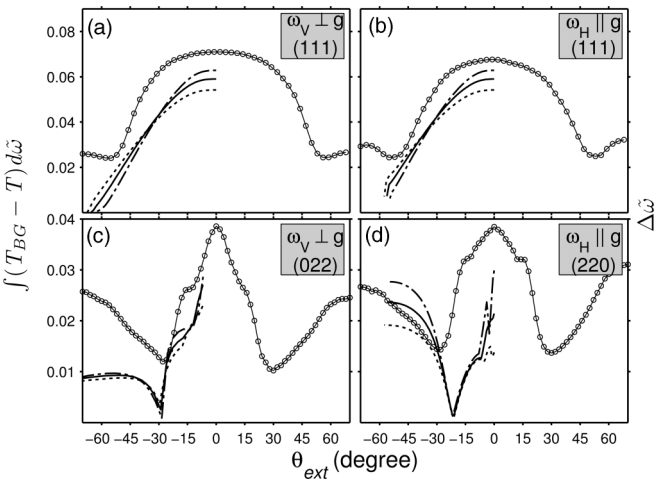

FIG. 9. The I_{TD} and the theoretical gap width for three different peaks and geometries as indicated. The different theoretical curves have been calculated from band structures for opals with a radius of 0.49D (dash-dotted line), 0.50D (solid line), and 0.51D (dotted line). The ideal close-packed opal has a radius of 0.50D.

Therefore the (022) ridge corresponds to gap between 8th and the 9th bands.

The comparison of the width of the partial gap and measured I_{TD} is shown in Fig. 9. For the peak corresponding to the stop band, there is a good qualitative agreement between measurement and calculation. The integrated intensity has a maximum at the L point and disappears near the W and $U(K)$ points. Ascribing a higher value to the background would shift the edge of the ridges slightly while the trend of transmission drop remains nearly unaffected. The slope of the theoretical curve decreases with the increase of the filling fraction (i.e., changing from expanded to close-packed or sintered opal models), however, there is not much change in its angular dependence.

An exciting nonmonotonous angular dependence of the I_{TD} was found for the (022)-type ridges as shown in Figs. 9(c) and 9(d). The initial decrease is followed by an increase with a shoulder. The theoretical value ($\Delta\tilde{\omega}$) was extracted from the band structure calculated along the $\Gamma^1\Gamma^2$ path for the case H and along $\Gamma^1\Gamma^{17}$ for the case V. The positions of the minima and the shoulder of the integrated intensities are in a fairly good agreement with the calculated values from the band structure. Here, it has to be considered that sometimes the separation of the regarded peak from other peaks is difficult. This can induce erroneous small shifts in the experimental curve. In our special case, the $(11\bar{1})$ ridge interferes with the (220) ridge. The characteristic features of the intensity curves are connected with degenerate states of the 6th, 7th, and 8th bands within the BZ for case H. In case V, degenerate states occur between the 8th and 9th bands. It is very likely that these features are not connected with further symmetry lines than the scanning line, but this question needs further investigation.

It is interesting that the calculated I_{TD} for (220) ridge shows a high sensitivity on the sphere packing conditions around $\theta_{ext} \approx 0$. A slight radius change results in a dramatic change on its shape. This sensitivity may enable a conclusive parameter fitting of refined opal models to the experimental results.

The visible deviations of the fit from the experimental data may come from four sources: (1) the I_{TD} integration boundaries, (2) an oversimplified sintering model, (3) the dispersion of the refractive index, and (4) the coupling factor between external and internal photon states. Due to the overlap of many ridges, it is difficult to unambiguously determine the edge of (022)-type transmission drops for external angles below 20 degrees. On the theoretical side, a more sophisticated description of the opal sintering than just the overlapping sphere model seems the most necessary to us.

E. Domain structure

The interpretation of ARS has required the consideration of the fcc structure twinning. Therefore, it is of some interest to have also information on size and arrangement of the different fcc domains. Our observation of stripes with different brightness under the microscope indicates that our opals consist of different domains which we assign to the two simultaneously formed fcc lattices.[28] The illumination direction determines which one of them has a bright appearance. The simultaneous probing of these domains due to the relatively large beam size in ARS is the reason of the highly symmetric ARS maps with respect to normal incidence.

The mechanism of image formation for the stripes seems to be rather complicated. On the one hand the stripes have the color of the Bragg reflection under the illumination angle. On the other hand, the Bragg reflection cannot reach the microscope objective because the objective's aperture is smaller than the illumination angle. Therefore scattering by defects must play a decisive role in the image formation. Clearly, a significant difference in the structure of the neighbored stripes must exist, otherwise they could not behave so differently. We assign this difference to the two possible fcc lattices with two corresponding defect distributions. The detailed explanation of the image formation will, however, be the topic of a separate paper. The stripes are oriented parallel to growth direction. We have observed that they have already been formed during deposition.

The existence of similarly regular stripes (width 50–300 μm) orientated along the growth direction on a VD-made opal film was reported by Andreani *et al.*[19] The image was taken in transmission mode at an oblique illumination. The authors interpreted the differently-colored stripes in a related manner. This result as well as the very similar lattice orientation[28,37] indicate a strong similarity in opal formation mechanisms between the VD and the CDM. In both methods, the suspension flow has a dominant influence on particle ordering.

V. CONCLUSIONS

The ARS maps show that CDM-made opals deliver well-resolved and rich patterns in the range of higher Bragg peaks. Such patterns have not been reported so far. In addition, the observation of Fabry-Perot oscillations indicates homogeneity of the opal samples.

Even though opal films look homogeneous, we found that they consist of alternating parallel stripes. The stripes correspond to differently oriented fcc domains with the

average width of 700 μm. This surprisingly high width points, in turn, to a negligible effect of the corresponding domain boundary in many experiments. The existence of the fcc1|fcc2 domain boundary was already concluded in a former paper,[28] but their importance for the optical properties was slightly overestimated.

The kinematical interpretation of ARS maps explains the observed ridges very well. Furthermore, the refractive index dispersion turns out to be important for discussing high-order diffraction ridges. The band structures deliver a convincing explanation of the intensity variation of selected low-order ridges.

The transmission drop of the (220) peak in H geometry was found to be very sensitive on sphere sintering; its shape changes significantly by a slight change in sphere packing (non-close-packed or sintered). This can be used for deeper exploration of sintering or deformation of artificial opals.

ACKNOWLEDGMENTS

The authors would like to thank A. Krappweis and D. Marlow for reading the manuscript and C. Lehmann for helpful discussions. We acknowledge the IMPRS for Surface and Interface Engineering in Advanced Materials (SurMat) and the European Union and the Ministry of Innovation, Science, and Research (Objective 2 program ERDF) for the support.

*To whom correspondence should be addressed: marlow@mpi-muelheim.mpg.de

[1] M. Notomi, Rep. Prog. Phys. **73**, 1 (2010).
[2] H. Kosaka, T. Kawashima, A. Tomita, M. Notomi, T. Tamamura, T. Sato, and S. Kawakami, Appl. Phys. Lett. **74**, 1212 (1999).
[3] H. Kosaka, T. Kawashima, A. Tomita, M. Notomi, T. Tamamura, T. Sato, and S. Kawakami, Phys. Rev. B **58**, R10096 (1998).
[4] T. Prasad, V. Colvin, and D. Mittleman, Phys. Rev. B **67**, 165103 (2003).
[5] C. Luo, S. G. Johnson, M. Soljačić, J. D. Joannopoulos, and J. B. Pendry, Proc. SPIE **5166**, 207 (2004).
[6] Y. A. Vlasov, V. N. Astratov, A. V. Baryshev, A. A. Kaplyanskii, O. Z. Karimov, and M. F. Limonov, Phys. Rev. E **61**, 5784 (2000).
[7] M. S. Thijssen, R. Sprik, J. E. G. J. Wijnhoven, M. Megens, T. Narayanan, A. Lagendijk, and W. L. Vos, Phys. Rev. Lett. **83**, 2730 (1999).
[8] M. V. Rybin, K. B. Samusev, and M. F. Limonov, Phys. Solid State **50**, 436 (2008).
[9] F. García-Santamaría, J. F. Galisteo-López, P. V. Braun, and C. López, Phys. Rev. B **71**, 195112 (2005).
[10] E. Pavarini, L. C. Andreani, C. Soci, M. Galli, F. Marabelli, and D. Comoretto, Phys. Rev. B **72**, 045102 (2005).
[11] H. Míguez, V. Kitaev, and G. A. Ozin, Appl. Phys. Lett. **84**, 1239 (2004).
[12] J. F. Galisteo-López, E. Palacios-Lidón, E. Castillo-Martínez, and C. López, Phys. Rev. B **68**, 115109 (2003).
[13] H. M. van Driel and W. L. Vos, Phys. Rev. B **62**, 9872 (2000).
[14] W. L. Vos and H. M. van Driel, Phys. Lett. A **272**, 101 (2000).
[15] S. G. Romanov, T. Maka, C. M. Sotomayor Torres, M. Müller, R. Zentel, D. Cassagne, J. Manzanares-Martinez, and C. Jouanin, Phys. Rev. E **63**, 056603 (2001).
[16] R. Fujikawa, A. V. Baryshev, K. Nishimura, H. Uchida, and M. Inoue, J. Porous Mater. **13**, 287 (2006).
[17] A. V. Baryshev, A. B. Khanikaev, R. Fujikawa, H. Uchida, and M. Inoue, J. Mater. Sci: Mater. Electron. **20**, S416 (2009).
[18] S. G. Romanov, M. Bardosova, I. M. Povey, M. E. Pemble, and C. M. S. Torres, Appl. Phys. Lett. **92**, 191106 (2008).
[19] L. C. Andreani, A. Balestreri, J. F. Galisteo-López, M. Galli, M. Patrini, E. Descrovi, A. Chiodoni, F. Giorgis, L. Pallavidino, and F. Geobaldo, Phys. Rev. B **78**, 205304 (2008).
[20] M. Ishii, M. Harada, A. Tsukigase, and H. Nakamura, Colloids and Surfaces B: Biointerfaces **56**, 224 (2007).
[21] A. Balestreri, L. C. Andreani, and M. Agio, Phys. Rev. E **74**, 036603 (2006).
[22] J. F. Galisteo-López and C. López, Phys. Rev. B **70**, 035108 (2004).
[23] D. Comoretto, E. Pavarini, M. Galli, C. Soci, F. Marabelli, and L. C. Andreani, in *Proceedings of SPIE*, edited by P. M. Fauchet and P. V. Braun, Vol. 5511 (SPIE, Bellingham, WA, 2004).
[24] R. V. Nair and R. Vijaya, Phys. Rev. A **76**, 053805 (2007).
[25] M. V. Rybin, K. B. Samusev, and M. F. Limonov, Photon. Nanostructures **5**, 119 (2007).
[26] S. A. Asher, J. M. Weissman, A. Tikhonov, R. D. Coalson, and R. Kesavamoorthy, Phys. Rev. E **69**, 066619 (2004).
[27] H.-L. Li, W. Dong, H.-J. Bongard, and F. Marlow, J. Phys. Chem. B **109**, 9939 (2005).
[28] M. Muldarisnur and F. Marlow, J. Phys. Chem. C **115**, 414 (2011).
[29] S. G. Johnson and J. D. Joannopoulos, Opt. Express **8**, 173 (2001).
[30] F. Marlow, M. Muldarisnur, P. Sharifi, R. Brinkmann, and C. Mendive, Angew. Chem. Int. Ed. **48**, 6212 (2009).
[31] See Supplemental Material at http://link.aps.org/supplemental/10.1103/PhysRevB.86.024105 which presents a comparison between ARS maps and band structures as well as details on solving Bragg law for a dispersive material.
[32] J. Als-Nielsen and D. McMorrow, *Elements of Modern X-ray Physics* (Wiley, New York, 2011).
[33] B. Lange, J. Wagner, and R. Zentel, Macromol. Rapid Commun. **27**, 1746 (2006).
[34] Y. A. Vlasov, M. Deutsch, and D. J. Norris, Appl. Phys. Lett. **76**, 1627 (2000).
[35] T. Ochiai and J. Sanchez-Dehesa, Phys. Rev. B **64**, 245113 (2001).
[36] N. W. Ashcroft and N. D. Mermin, *Solid State Physics* (Harcourt College Publisher, Orlando, 1976).
[37] K. Wostyn, Y. Zhao, B. Yee, K. Clays, A. Persoons, G. d. Schaetzen, and L. Hellemans, J. Chem. Phys. **118**, 10752 (2003).